CrystEngComm

Accepted Manuscript

ROYAL SOCIETY OF CHEMISTRY

www.rsc.org/crystengcomm

Highly Efficient Cyan-Emitting Garnet Phosphor $Ca_3Hf_2SiAl_2O_{12}$: xCe^{3+} for Solid State White Lighting

Xin Ding, Ge Zhu, Wanying Geng, Qian Wang, Yuhua Wang*

Department of Materials Science, School of Physical Science and Technology, Lanzhou University

Key Laboratory of Special Function Materials and Structure Design, Ministry of Education, Lanzhou University, Tianshui South Road No. 222, Lanzhou, Gansu 730000, PR China

Abstract

In this paper, we have synthesized a new garnet compound $Ca_3Hf_2SiAl_2O_{12}$ and a series of Ce^{3+}-doped phosphor $Ca_3Hf_2SiAl_2O_{12}$: xCe^{3+}. The crystal structure and luminescence properties of the $Ca_3Hf_2SiAl_2O_{12}$: xCe^{3+} were investigated in detail. Transmission electron microscopy analysis and XRD Rietveld refinement show that $Ca_3Hf_2SiAl_2O_{12}$ belongs to body-centered cubic and Ia-3d (230) space-group with a = 12.3666 Å. $Ca_3Hf_2SiAl_2O_{12}$: xCe^{3+} took on broad excitation bands at 330 and 400 nm attributed to Ce^{3+} characteristic 5*d*-4*f* transition and can emit cyan emission under 400 nm UV light excitation. The emission intensity of CHSA: 1%Ce^{3+} phosphor can reach to 68.9% of YAG: Ce^{3+} (commercial) and 72.1% of $Ca_8Mg(SiO_4)_4Cl_2$: Eu^{2+} (commercial). The average decay lifetimes of $Ca_3Hf_2SiAl_2O_{12}$:1%Ce^{3+} is 48.91 ns, which is consistent with its nanosecond peculiarity of Ce^{3+}. In the process of increasing the temperature from 25 °C to 250 °C, the integrated emission intensity of $Ca_3Hf_2SiAl_2O_{12}$:0.5%Ce^{3+} is only decreased to 57.8% (250 °C) and shows nice thermal stability comparing with commercial YAG: Ce^{3+}(P46-Y3). Furthermore, $Ca_3Hf_2SiAl_2O_{12}$: 0.5%Ce^{3+} exhibits outstanding quantum efficiency (74.7%). It reveals that $Ca_3Hf_2SiAl_2O_{12}$: xCe^{3+} possesses remarkable optical properties and can be utilized in UV-LEDs.

Keywords: TEM, XRD, Structure, Phosphor, Luminescence

*Corresponding author at: Department of Materials Science, School of Physical Science and Technology, Lanzhou University, Lanzhou, 730000, PR China.

Tel.: +86 931 8912772; fax: +86 931 8913554.

Corresponding author' email: wyh@lzu.edu.cn

1. Introduction

Materials with garnet structure and their solid solutions have been become attentive new functional materials and have been widely used in many areas. Typically, $Bi_3Fe_4Ga_1O_{12}$, $Gd_3Fe_5O_{12}$: Bi, $Li_6ALa_2Nb_2O_{12}$ (A = Ca, Sr, Ba), $Y_3Al_5O_{12}$: Er, $Y_3Al_5O_{12}$: Nd, $Y_3Al_5O_{12}$: Yb, $Y_3Al_5O_{12}$: Ce have been utilized in laser, magnetic, magneto-optic, optical circulator, ion conductors and white light-emitting diodes (LEDs) etc. [1-8]. Among them, white-LEDs, with the advantages of high light efficiency, low energy consumption, long service lifetime and environmentally friendly have drawn much attention because of their wide applications [9-11]. Garnet structure compounds are stable from chemical and photochemical points of view. Therefore, phosphors possessing garnet crystal structure are highly desirable. White-LEDs can be as the potential replacements for conventional light sources. Most of the Ce^{3+} doped inorganic compounds usually absorb in the UV–blue spectral region. However, the garnet crystal structure

generates strong crystal-field strength on the dodecahedral site where Ce^{3+} ions are located; therefore, the emission can be shifted to the green, yellow, or even orange-red spectral regions depending on the lattice composition. Since luminescent properties can be determined by structure, many researchers have spent a lot of effort with garnet and developed some phosphors with garnet structure such as $Ca_3Sc_2Si_3O_{12}:Ce^{3+}$ (green), $Lu_2CaMg_2(Si,Ge)_3O_{12}:Ce^{3+}$ (yellow), $Gd_3Al_5O_{12}$: Dy^{3+}, Lu^{3+} (orange-red) [12-14]. At present, the most widely used commercial phosphor to produce White-LEDs is $Y_3Al_5O_{12}$: Ce (YAG: Ce), which is an artificial compound developed from $\{C\}_3[A]_2(D)_3O_{12}$ garnet system [15]. Blue LED radiation is strongly absorbed by the allowed 4*f*-5*d* transition of Ce^{3+}, leading to a yellow 5*d*-4*f* (to the spin-orbit split $^2F_{7/2}$ and $^2F_{5/2}$ levels) emission band in YAG: Ce^{3+}. The combination of the yellow YAG: Ce emission and blue radiation blending through the phosphor coating gives white light. However, different degradation for blue chip and phosphor leads to chromatic aberration. Lack of red light component causes high correlated color temperature (CCT) (7765 K), poor color rendering index and thermal quenching properties which restricts the use of these LEDs in many general lighting applications, especially as replacements for lamps that need lower CCT that make up the majority of the lighting market [16-19]. By co-doped Mn^{2+} in YAG: Ce, the CCT can reach to 3700 K, but, the emission intensity is too weak to meet application [20, 21]. Consequently, near-ultraviolet LEDs (n-UV LEDs) combined with multi-component phosphors were devolved in view of their superior light quality, color uniformity, and high colorrendering index (CRI, Ra) [22-24]. A new species of the garnet super-group $Ca_3(Hf, Sn, Zr, Ti)_2SiAl_2O_{12}$ was discovered in metasomatically altered carbonate-silicate xenoliths in ignimbrites of the upper Chegem Caldera, Northern Caucasus, Kabardino-Balkaria, Russia at 2013 [25]. It is said that Hf-garnet obtains higher in the conduction band, above 4.0 eV [26], which may obtain NUV excitation. To our best knowledge, there are no researches of its synthesis and photoluminescence which have been reported. Therefore, in this work, we try to synthesize Hf-garnet and Ce^{3+}-doped phosphors, then, investigated their structure and photoluminescence properties and find that it is potentially applicable to n-UV white LEDs.

2. Experimental Section

2.1 Materials and utensil $CaCO_3$ (99.9%), HfO_2 (99.99%), H_2SiO_3 (AR), $Al(OH)_3$ (AR) and CeO_2 (99.99%) as the raw materials are stoichiometric and 5wt% H_3BO_3 as the flux is also used in the synthesis process. Aluminum oxide crucibles (10 mm*10 mm) and porcelain boat are utensils for sintering.

2.2 Synthesis

A series of $Ca_3Hf_2SiAl_2O_{12}$: xCe^{3+}(x = 0.5-5%) samples are synthesized by two-step traditional high temperature solid-sated reaction. The relative amounts of materials are calculated and then are weighed by electronic balance accurate to 4 decimal places. Put all the raw materials and the flux into agate mortar with 8 mL ethanol added in it at the same time. Grind the mixture for 30 min until they are evenly blended and homogeneous. After the mixture dry, transfer the mixture into aluminum oxide crucibles (10 mm*10 mm) and pre-fire at 800 °C for 2 h under air atmosphere, then, calcine them at 1480 °C for 6 h under flowing 95% N_2−5% H_2 atmosphere in the horizontal tube furnace. When they are cooled with 5 °C /min speed to room temperature, grind them to powders, yielding the resulting phosphor powder.

2.3 Characterization

HRTEM (High-resolution transmission electron microscopy) and FFT (Fast Fourier transform) pattern measurements are carried out on a transmission electron microscope at an operating

voltage of 200 kV. The phase formation and crystal structure were analyzed by the X-ray powder diffraction (XRD) (D2 PHASER X-ray Diffractometer ,Germany) with graphite monochromator using Cu Kα radiation（λ = 1.54056 A), operating at 30 kV and 15 mA. The investigation range is 10 ° to 80 ° with scanning speed of 15 ° 2θ min^{-1} for the series $Ca_{3-x}CeHf_2SiAl_2O_{12}$ ($0.015 \leq x \leq 0.15$) samples and 10 °-90 ° with 2 ° 2θ min^{-1} for the structural refinement data. The photoluminescence (PL) and photoluminescence excitation (PLE) spectra of the samples are measured by a Fluorlog-3 spectrofluorometer equipped with 450 W xenon lamps (Horiba Jobin Yvon). The temperature-dependence luminescence properties are measured on the same spectrophotometer, which is combined with a self-made heating attachment and a computer-controlled electric furnace from room temperature (25 ℃) to 250 ℃ with a heating rate of 100 ℃/min and a holding time of 5 min for each temperature point. Photoluminescence quantum efficiency is measured by FLS-920T fluorescence spectrophotometer equipped with a 450W xenon light source. The luminescence decay curves were obtained by FLS-920T fluorescence spectrophotometer as well. All the testes are carried out at room temperature.

3. Results and discussion

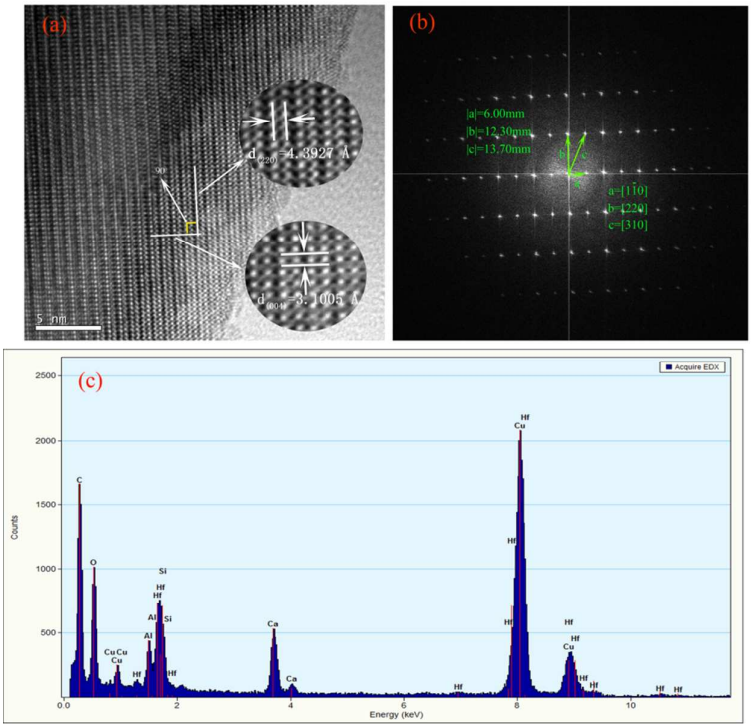

Figure 1: (a) HRTEM image; (b) FFT image; (c) EDX (energy-disperse x-ray analysis)

3.1 Composition and structural characteristics of $Ca_3Hf_2SiAl_2O_{12}$

The structure and composition of the $Ca_3Hf_2SiAl_2O_{12}$ (CHSA) were well examined by HRTEM, FFT, EDX. In Figure 1a, there are two apparent interplanars belong to (220) and (004) according to the calculation and measurement which are vertical to each other. The HRTEM image reveals that $Ca_3Hf_2SiAl_2O_{12}$ takes on characteristic preferred orientation yielding by solid-state reaction which can be certificated with two relatively strong peaks in XRD patterns (shown in Figure 4). FFT image is punctate distribution cause to homogeneous and preferred crystalline in the HRTEM area. In FFT image,$|a|^2 : |b|^2 : |c|^2 = 36 : 156.25 : 196 \approx 2 : 8 : 10$, in general speaking,

body-centered cubic crystal system possesses this kind ratio. It can obtain that the three crystal orientations are $a = [1\bar{1}0]$, $b = [220]$ and $c = [310]$. That can be as a testimony of $Ca_3Hf_2SiAl_2O_{12}$ belonging to body-centered cubic and Ia-3d (230) space-group. The chemical composition of this compound is further determined by EDX as shown in Figure. 1c. The signals of calcium (Ca), hafnium (Hf), oxygen (O), silicon (Si) and aluminum (Al) suggest the presence of the corresponding element in the product (the carbon and Cu signal are due to the instrument).

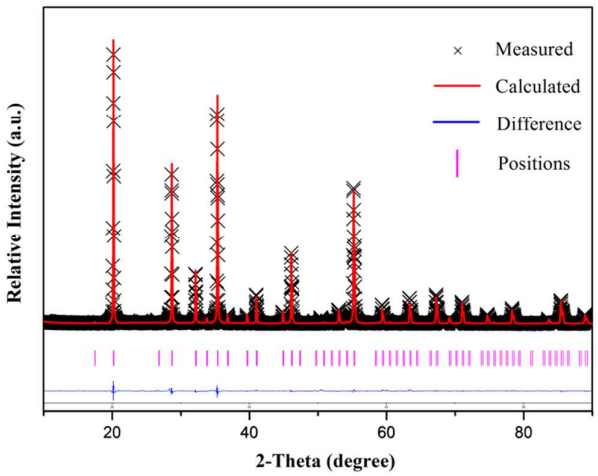

Figure 2 Rietveld refinement of the powder XRD profile of CHSA

Table 1 Structural parameters of CHSA as determined by the rietveld refinement of Powder XRD data at room temperature

$Ca_3Hf_2SiAl_2O_{12}$				formula weight	2924.29g/mol
atom(site)	x	y	z	Crystal system	cubic
Ca	1/8	0	1/4	Space-group	Ia-3d(230)
Hf	0	0	0	Cell parameters	a = 12.3666 Å
Si	3/8	0	1/4	Cell volume	1891.26 $Å^3$
Al	3/8	0	1/4	Calc. density	2.5674 g/cm^3
O	0.03401	0.04837	0.66102	Z	8

In order to determine the real structure of the synthesized samples, ICSD-100258 ($Ca_{2.94}Mg_{0.38}Zr_{1.21}Ti_{0.47}(Si_{1.61}AlFe_{0.39})O_{12}$) was used as the standard data to refine CHSA and structural refinement of XRD was made using Materails Studio program. Figure 2 illustrates the experimental and refined XRD patterns of CHSA sample. The "×" marks represent the measured diffraction data. The red solid curves indicate the calculated diffraction data and the pink vertical lines show the positions of the simulated diffraction patterns. The blue solid line denotes the deviation between the measured and calculated values. By comparing the calculated data with the experimental spectra, we found that each peak is in good agreement. There is no impurity phase found in the samples, which reveals that it is good single-phase. The calculated residual factor value is Rp = 6.97%, and Rwp = 9.99%. Table 1 lists the refinement data of CHSA.

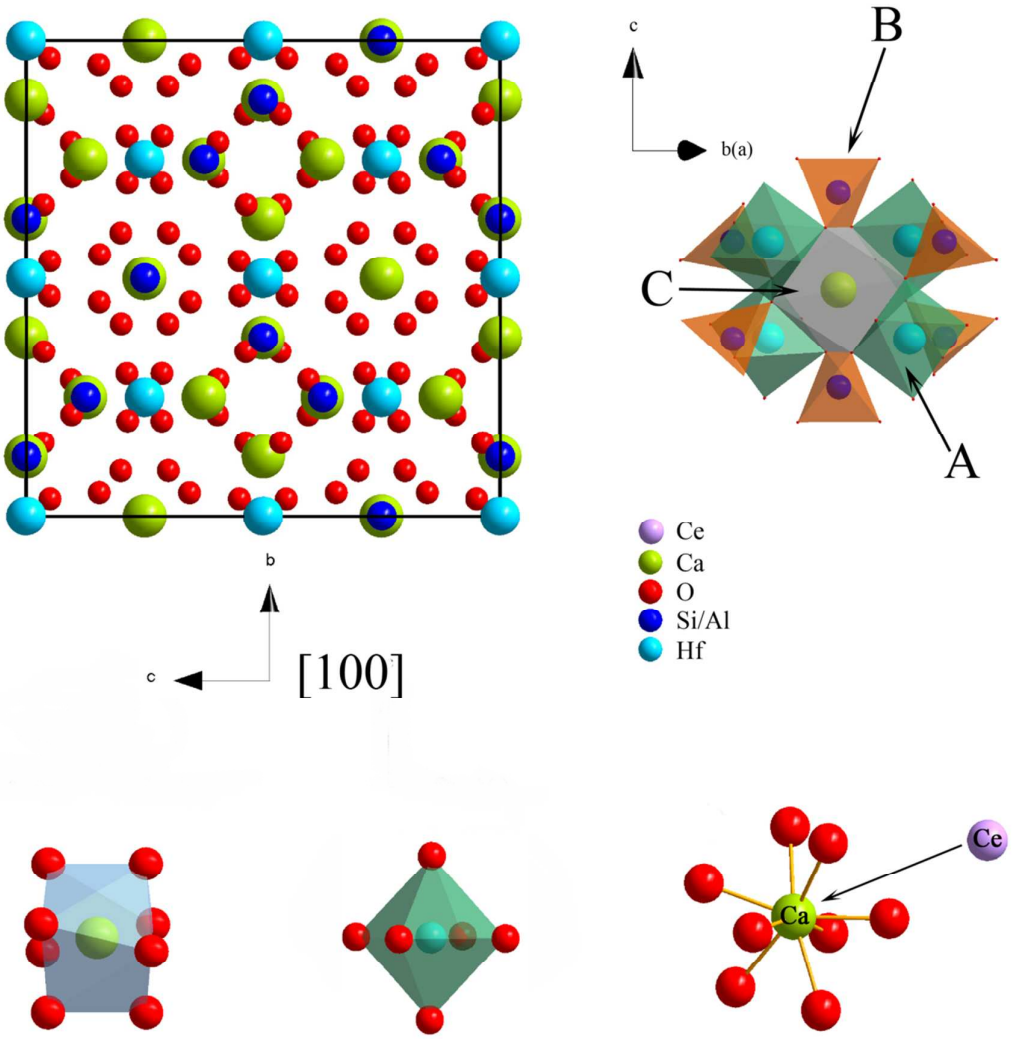

Figure 3 The structure of garnet ($Ca_3Hf_2SiAl_2O_{12}$) and the coordination environment of Ca^{2+}.

$Ca_3Hf_2SiAl_2O_{12}$ belongs to body-centered cubic crystal system and Ia-3d (230) space-group which is shown in Figure 3(1) observing from [100] crystal orientation. In the present work, there is valency imposed double site-occupancy (R^{4+}, R^{3+}) at the B site [25, 27], which Al and Si atoms are in substitutional disorder, and the atomic position and anisotropic displacement parameters of Al and Si are constrained to be identical at Al/Si sites in the initial refinements. There is only one lattice site for Hf, Al/Si and Ca, respectively. The A site (green octahedrons, $[HfO_8]^{4-}$) is fully occupied by Hf, while the B site (orange tetrahedrons, $[AlO_4]^{5-}$, $[SiO_4]^{4-}$) is occupied by 2/3 Al and 1/3 Si. Small light green spheres located in the space between the polyhedrons represent the C site which is occupied by Ca. The anion sites (oxygen sites) are located at the shared corners of the octahedra and tetrahedra. In addition, in this similar structure, A site (Figure 3(4)) can be also occupied by Ti, Zn or Sn. A significant difference between the Ti-based garnet and the Zr and Hf based one is related to the location of the transition metal d states in the band structure. While the Ti d band is located close to the bottom of the conduction band [between ~2.0 and ~4.0 eV], the Zr and Hf d states are located higher in the conduction band, above 4.0 eV, which may obtain n-UV excitation. This must be traced to the considerable mismatch between the energies of Ti d orbitals (−11.05 eV) as compared with the Zr and Hf d (−8.46 and −8.14 eV) orbitals [25]. Due to

the low symmetry of the garnet structure, after the atomic relaxation, the cations are slightly displaced from their ideal positions, and the oxygen atoms in a certain coordination shell are not located at the same distance from the cation.

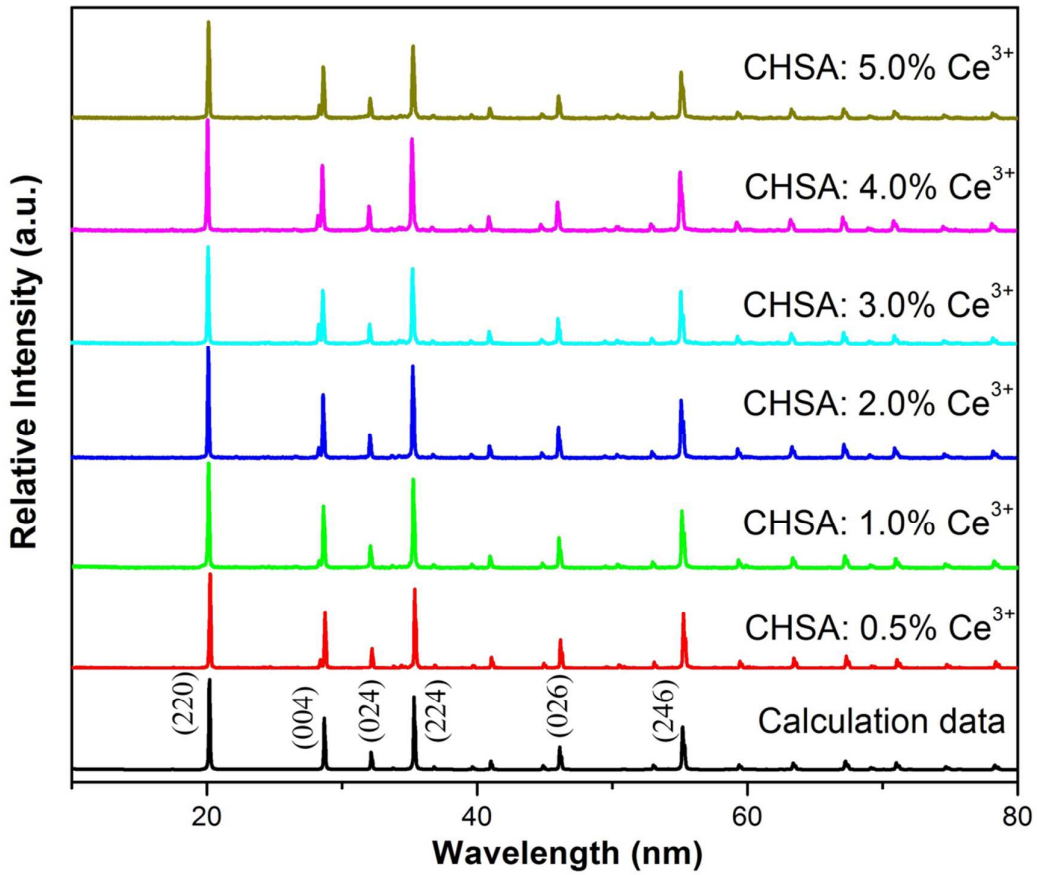

Figure 4 XRD patterns of series CHSA: x%Ce^{3+} and calculated data.

3.2 XRD analysis of series CHSA: x%Ce^{3+}

XRD patterns of the as-prepared CHSA: x%Ce^{3+} (x = 0.5 1, 2, 3, 4, 5) phosphors were collected to verify the phase purity. As is given in Figure 4, it can be seen that all of the diffraction peaks of the samples can be basically indexed to the corresponding calculated data (Rietveld refinement data), suggesting that $Ca_{3-x}Ce_xHf_2SiAl_2O_{12}$ with different Ca/Ce ratios can be formed in the single-phased structure. In the meantime, the diffraction peaks shift to smaller angles with increasing Ce^{3+} content owing to the different ionic radius between Ca^{2+} and Ce^{3+}, indicating that Ce^{3+} have been doped into the crystal lattices of the cubic $Ca_3Hf_2SiAl_2O_{12}$ instead of forming the impurity phase.

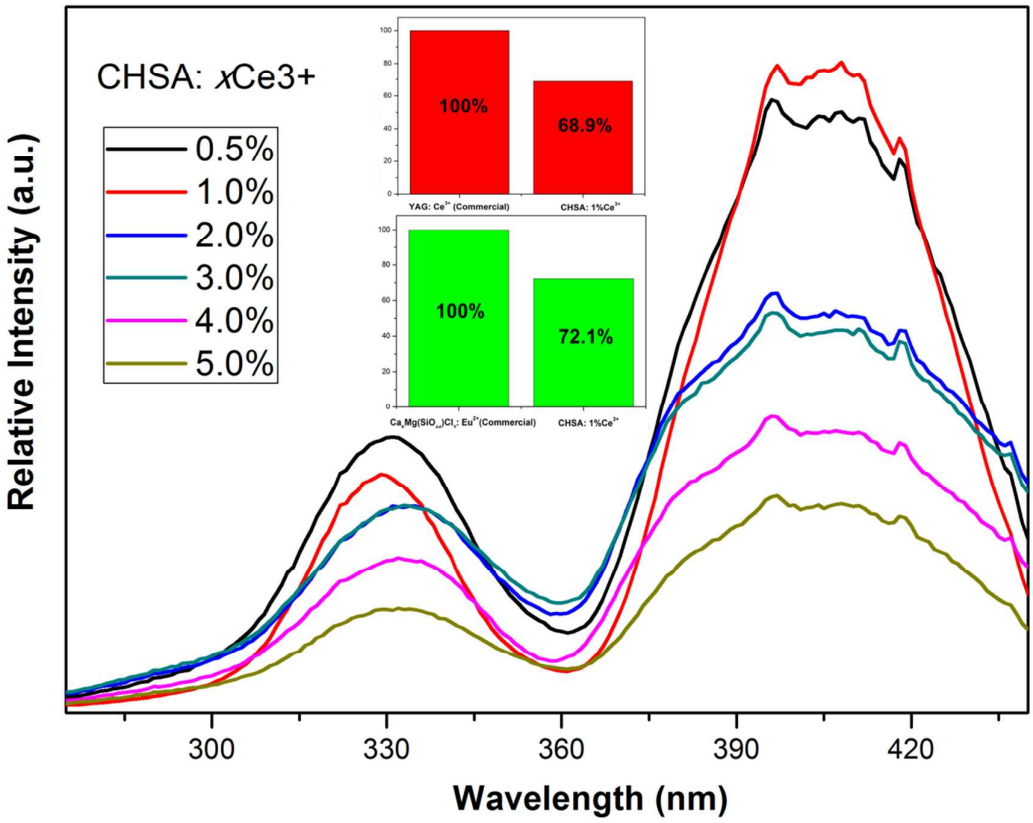

Figure 5 Photoluminescence excitation properties with 1 nm slit of series CHSA: x%Ce^{3+}phosphors; Inset: Emission intensity comparing with percentage: (Red) YAG: Ce^{3+} (commercial) and CHSA: 1%Ce^{3+}; (Green) $Ca_8Mg(SiO_4)_4Cl_2$: Eu^{2+} and CHSA: 1%Ce^{3+}

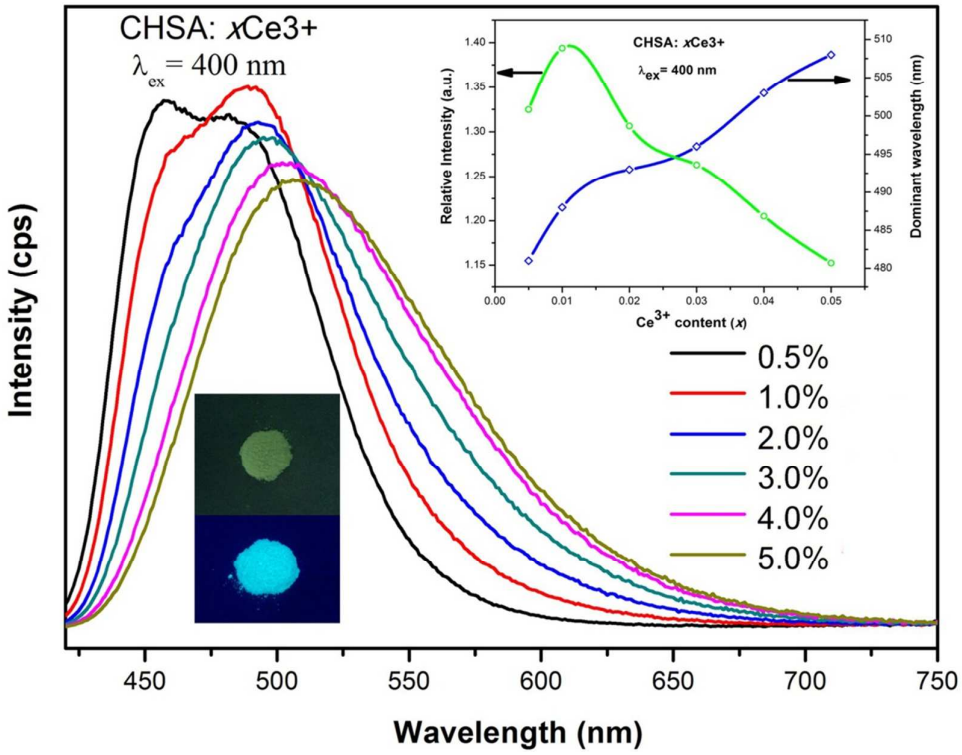

Figure 6 Photoluminescence properties under 400 nm excitation with 1 nm slit of series CHSA: x%Ce^{3+} phosphors; Inset: (Upper right) Dependence of emission intensity and peak position of CHSA: x%Ce^{3+} phosphors on Ce^{3+} content; (lower left) CHSA: 1%Ce^{3+} powder and its image under UV excitation

3.3 Luminescence properties of CHSA: $x$$Ce^{3+}$

The PLE and PL spectra of CHSA: $x$$Ce^{3+}$ (x = 0.005, 0.01, 0.02, 0.03, 0.04, 0.05) excited by 400 nm and monitored at 480-505 nm are depicted in Figure 5 and Figure 6. The PLE spectra exhibit two distinct excitation bands at 330 and 400 nm, which could be ascribed to the electronic transitions from the ground 4f state to the different crystal field splitting bands of excited 5d states of Ce^{3+} [28, 29]. The inset of Figure 5 shows that the emission intensity of CHSA: 1%Ce^{3+} phosphor can reach to 68.9% of YAG: Ce^{3+} (commercial) and 72.1% of $Ca_8Mg(SiO_4)_4Cl_2$: Eu^{2+} (commercial) at the same text conditions. It can be seen that CHSA: $x$$Ce^{3+}$ can emit cyan light (450-550 nm) under UV excitation and the emission spectra consist of two apparent asymmetric broad peaks before x =0.03 which corresponds to the *5d–4f* allowed transition of Ce^{3+}, beyond x =0.03, emission spectra turn to be a broad peak. Additionally, the inset (upper right) of Figure 6 shows the Ce^{3+} content dependent emission intensity and peak position. It can be easily seen that the emission intensities have an obvious increasing trend with increasing Ce^{3+} concentration, and maximizes at x = 0.01, then the emission intensity decreases. The peak position has apparent red shift from 481 to 508 nm about 1105 cm^{-1}.

It is well-known that the typical emission of Ce^{3+} should consist of a double band in view of the transitions of Ce^{3+} ions from 5*d* state to the $^2F_{5/2}$ and $^2F_{7/2}$ ground states. That's the reason why emission spectra consist of two apparent asymmetric broad peaks, and, with the increasing of Ce^{3+} content, the energy transfer of intra-Ce^{3+} becomes to be significant, this kind energy transfer that also leads to red shift and broader of emission and excitation spectra [30-32]. However, in CHSA

host, the relative larger dopant Ce^{3+} (radius = 1.283 Å for eight coordinated) occupies Ca^{2+} (radius = 1.26 Å for eight coordinated) site will lead to contradictory results (blue shift) of emission spectra [33].

$$D_q = \frac{1}{6} Ze^2 \frac{r^4}{R^5}$$

Where Dq is a measure of the energy level separation, Z is the anion charge, e is the electron charge, r is the radius of the d wavefunction, and R is the bond length. When the Ca^{2+} ion is substituted and occupied by a larger Ce^{3+} ion (radius = 1.283 Å), the distance between the Ce^{3+} and O^{2-} ion becomes larger. Since crystal field splitting is proportional to $1/R^5$, this larger Ce^{3+}-O^{2-}distance also leads to the weakening of crystal field strength surrounding the Ce^{3+} ion and further results in a samller crystal field splitting of Ce^{3+} 5*d* energy levels, which makes the lowest 5*d* state of Ce^{3+} further to its ground state and finally gives a blue shift of the PL emission peak of the Ce^{3+}. Energy transfer of intra-Ce^{3+} and crystal field splitting may affect PL emission shift together and the former is dominated. Additional, the emission spectrum is composed of two broad bands cause to the characteristic transitions of Ce^{3+} ions from 5*d* state to the $^2F_{5/2}$ and $^2F_{7/2}$ ground states. With the increasing of Ce^{3+} content, the relative high energy transitions (5d to $^2F_{5/2}$) decays faster than another energy transitions (5d to $^2F_{7/2}$) due to the energy transfer between these two emissions. That leads to apparent shape changes of emission spectra. The emission intensity ratio of 5d-$^2F_{5/2}$ to 5d-$^2F_{7/2}$ tends to decrease with the doping concentration. When the concentration of Ce^{3+} ions is low (such as $x = 0.005$), the emission of 5d-$^2F_{5/2}$ shows a higher intensity; in contrast, higher emission intensity of 5d-$^2F_{7/2}$ is found when the concentration of Ce^{3+} ions is high (such as x = 0.05). We think that the partial spectroscopic overlap between the lowest excitation band and the 5d-$^2F_{5/2}$ emission band (self-absorption) can interpret this phenomenon (see figure 5 and 6). When the doping concentration increases, the distance between adjacent Ce^{3+} ions becomes shorter. As a consequence, the energy transfer between adjacent Ce^{3+} ions is expected to be with a higher efficiency. An efficient energy transfer means that the 5d-$^2F_{5/2}$ emission from one Ce^{3+} will be absorbed by another adjacent Ce^{3+} with more efficiency, so the 5d-$^2F_{5/2}$ emission intensity is weaker for higher doping samples.

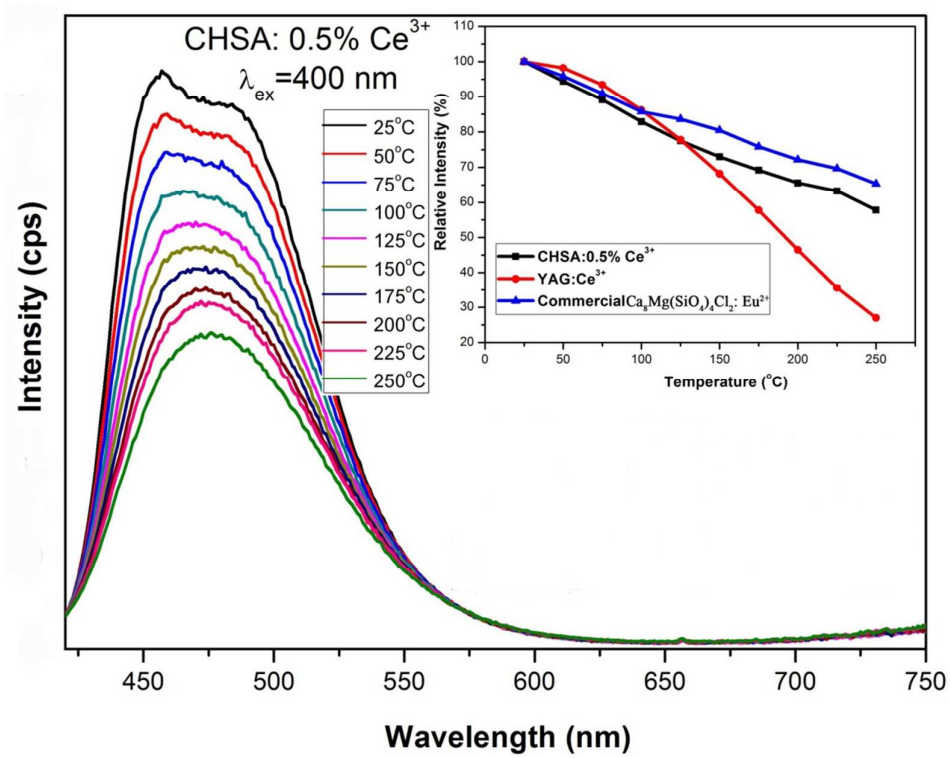

Figure 7 Temperature dependence of CHSA: 0.5%Ce^{3+} PL properties; Inset: contradistinction of CHSA: 0.5%Ce^{3+}, YAG: Ce^{3+} (P46-Y3, yellow phosphor) and commercial $Ca_8Mg(SiO_4)_4Cl_2$: Eu^{2+} (green phosphor).

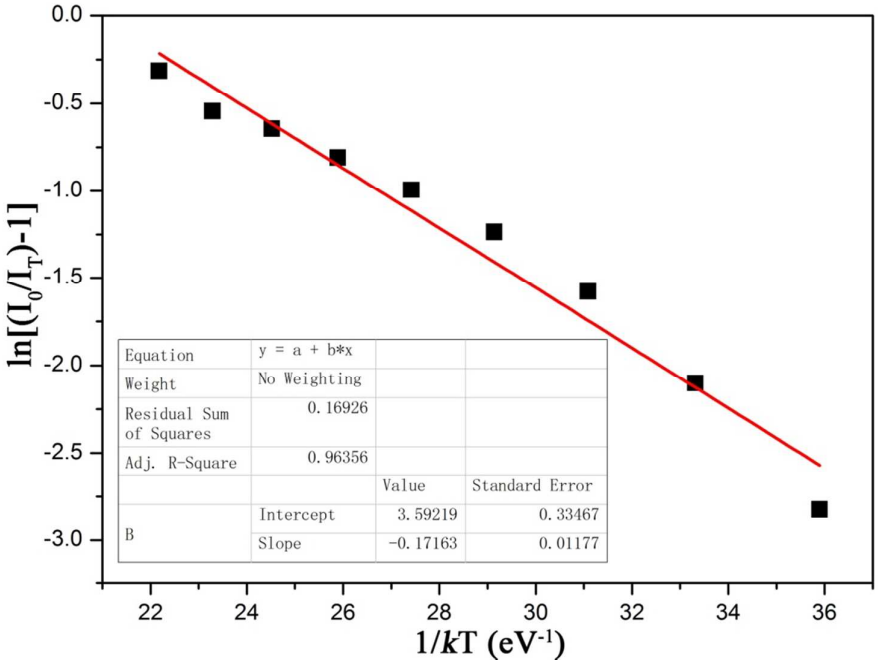

Figure 8 The Arrhenius fitting of the emission intensity of CHSA: 0.5%Ce^{3+} phosphor and the calculated Ea for thermal quenching

3.4 Thermal stability of CHSA: 0.5%Ce^{3+}

Temperature-dependent relative emission intensity under 400 nm excitation of CHSA: 0.5%Ce^{3+} is indicated in Figure 7. And the contradistinction of CHSA: 0.5%Ce^{3+}, YAG: Ce^{3+} (P46-Y3, similar garnet structure) and commercial $Ca_8Mg(SiO_4)_4Cl_2$: Eu^{2+} (green phosphor) are also investigated, which are shown in inset. It can be clearly seen that with temperature increasing, the emission intensity decreases gradually and the emission band goes from two apparent asymmetric broad peaks to one broad band definitely. Generally, the thermal quenching of emission intensity can be explained by a configurational coordinate diagram in which, through phonon interaction, the excited luminescence center is thermally activated through the crossing point between the excited state and the ground state. This non-radiative transition probability by thermal activation is strongly dependent on temperature resulting in the decrease of emission intensity [34, 35]. Due to the increasing phonon interaction and non-radiative transition with increasing temperature, the spectral overlap between the excitation band (Figure 5 and 6) and the first emission band (5d-$^2F_{5/2}$ emission band) increases. This results in more re-absorption of the first emission due to the 5d-$^2F_{5/2}$ transition and thus in a relative stronger decrease of the 458 nm with respect to the 481 nm emission band. That leads to two apparent asymmetric broad peaks to one broad band definitely with temperature increasing. In the process of increasing temperature from 25 °C to 250 °C, the integrated emission intensity of CHSA: 0.5%Ce^{3+} is decreased to 57.8% (250 °C) of the initial value (25 °C), meanwhile, commercial $Ca_8Mg(SiO_4)_4Cl_2$: Eu^{2+} (green phosphor) and YAG: Ce^{3+} (P46-Y3, yellow phosphor) are decreased to 65.3% and 27%. It is demonstrated that the temperature-dependent properties of CHSA: 0.5%Ce^{3+} is better than YAG: Ce^{3+} (P46-Y3, yellow phosphor) and similar with $Ca_8Mg(SiO_4)_4Cl_2$: Eu^{2+}. Furthermore, it also takes on a slight red shift with temperature increasing what others work have mentioned [36]. At lower Ce^{3+} concentrations (x = 0.5%), the emission band of Ce^{3+} is mainly dominated by the transition of 5*d* to 4*f* (namely, intrinsic emission). The decrement of emission intensity with the increase of temperature can be ascribed to the temperature-dependent electron–phonon interaction. With the increase of temperature, the electron–phonon interaction increases, which further makes the electrons at the bottom of the 5*d* excited state and shift to the junction of the excited and ground states and then relax to the 4*f* ground state in a nonradiative way. The activation energy (Ea) was calculated using the Arrhenius equation [37]

$$I_T = \frac{I_0}{1+c\exp(-\frac{\Delta E}{kT})} \quad (5)$$

where I_0 is the initial PL intensity of the phosphor at room temperature, I_T is the PL intensity at different temperatures, c is a constant, ΔE is the activation energy, and k is the Boltzmann constant (8.62×10^{-5} eV). Making this function to do logarithmic transformation can get

$$\ln\left(\frac{I_0}{I_T} - 1\right) = c(-\frac{\Delta E}{kT}) \quad (6)$$

According to the equation, the activation energy ΔE can be calculated by plotting $\ln[(I_0/I_T)-1]$ against $1/kT$, where a straight slope equals ΔE. As shown in Figure 8, ΔE was found to be 0.17163eV

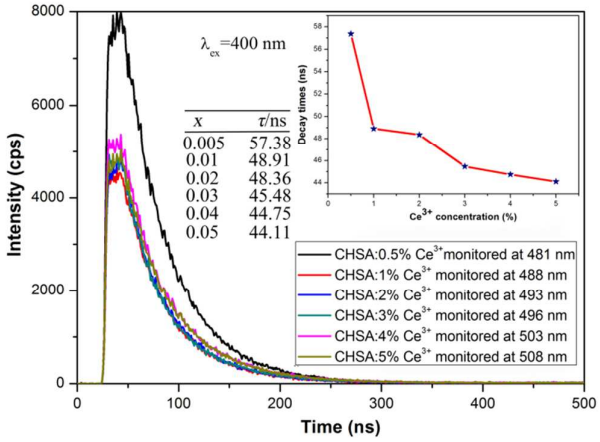

Figure 9 PL decay curves of CHSA: xCe^{3+} phosphors with 400 nm excitation; Inset: Dependence of decay time CHSA: x%Ce^{3+} phosphors on Ce^{3+} content.

3.5 PL decay curves and quantum efficiency of CHSA: xCe^{3+}

Figure 8 and the inset present the room temperature decay curves of the Ce^{3+} luminescence in CHSA: xCe^{3+} with different Ce^{3+} contents ($0.005 \leq x \leq 0.05$) upon excitation at 400 nm. The entire decay curve can be well fitted to a second-order exponential decay model because of transitions of Ce^{3+} ions from 5*d* state to the $^2F_{5/2}$ and $^2F_{7/2}$ ground states by the following equation [38]:

$$I(t) = A_1 \exp(-t/\tau_1) + A_2 (-t/\tau_2)$$

Where I is the luminescence intensity; A_1 and A_2 are constants; t is time; and τ_1 and τ_2 are the lifetimes for the exponential components. Further, the average lifetime constant (τ^*) can be calculated as:

$$\tau^* = (A_1\tau_1^2 + A_2\tau_2^2)/(A_1\tau_1 + A_2\tau_2)$$

The calculated average lifetimes of the Ce^{3+} of CHSA: xCe^{3+} (x = 0.005, 0.01, 0.02, 0.03, 0.04, 0.05) are 57.38, 48.91, 48.36, 45.48, 44.75 and 44.11 ns, respectively. As we know, the lifetime for Ce^{3+} ion is about nanosecond (ns); the relatively shorter lifetime is due to the allowed electric-dipole 5*d*–4*f* transition caused by the poor spatial overlaps between the 5*d* and 4*f* orbital. The decay times are in accordance with the most frequent value of the normal Ce^{3+} emission in solids. The lifetime decreases monotonically with the increase of the Ce^{3+} content, indicating an efficient energy transfer among Ce^{3+}.

Table 2 Quantum efficiency of CHSA: xCe^{3+}

Ce^{3+} concentration	0.5%	1%	2%	3%	4%	5%
Quantum efficiency	74.7	62.59	60.89	60.41	60.38	60.20

Photoluminescence quantum efficiency of CHSA: xCe^{3+} samples with different Ce^{3+} content are measured which are shown in Table 2. It can be seen that the sample with 0.5% Ce^{3+} dopant has very high quantum efficiency of 74.7%. Meanwhile, it possesses relatively good emission intensity. With the increasing content of Ce^{3+}, the quantum efficiency decreases gradually. However, CHSA: 1%Ce^{3+} sample with the highest emission does not obtain the highest quantum efficiency. Since the quantum efficiency depends closely on the some conditions, the particle size, morphology, and crystallization. In this system, Ce^{3+} substituting Ca^{2+} is no-equivalent displacement, which will produce some defects: each substitution of every two Ce^{3+} ion will create one vacancy defect V''_{Ca} with two negative charges, and two positive defects of $Ce^{\cdot}_{Ca}$ in the structure. The defects affect the photon absorbing of luminescent center (Ce^{3+}). Defects and concentration interaction

determine the photoluminescence quantum efficiency.

4. Conclusions

New garnet CHSA and a series of CHSA: xCe^{3+} phosphors were synthesized successfully by two steps high temperature solid-state reactions. The structure and composition were investigated detailed. CHSA belongs to body-centered cubic and Ia-3d (230) space-group with a = 12.3666 Å. CHSA: xCe^{3+} phosphor shows broad cyan emission at the range of 450 to 550 nm under UV excitation of 400 nm which could be matching the latest UV-chips well. The emission intensity of CHSA: 1%Ce^{3+} phosphor can reach to 68.9% of YAG: Ce^{3+} (commercial) and 72.1% of $Ca_8Mg(SiO_4)_4Cl_2$: Eu^{2+} (commercial). At the same test conditions, it has better thermal stability than YAG: Ce^{3+} and outstanding quantum efficiency (74.7%). It emerges nice optical properties and shows potential application in UV-LEDs.

Acknowledgment

This work is supported by Specialized Research Fund for the Doctoral Program of Higher Education (no. 20120211130003), the National Natural Science Funds of China (Grant no. 51372105) and the Fundamental Research Funds for the Central Universities (No. lzujbky-2014-231).

Reference

[1] S. Y. Kang, S. Z. Yin, V. Adyam, Q. Li, Y. Zhu, *IEEE Trans. Magnet.*, 2007, **43**, 3656

[2] G. Jacopo, P. Claudio, F. Antonella, R. M. Maria, P. Gaetano, *Otola. Head Neck Surge,* 2005 **133,** 923

[3] T.E. Jeffries, S. E. Jackson, H. P. Longerich, *J. Analy. Atom. Spectr.,* 1998, **13**, 935

[4] T. Mizumoto, K. Oochi, T. Harada, Y. Naito, *J. Light. Techn.,* 1986, **4**, 347

[5] V. Thangaduraiw, W. Weppner, *J. Am. Ceram. Soc.,* 2005, **88**, 411

[6] J. H. Park, J. K. Cho, K. Nishimura, H. Uchida, M. Inoue, *Phys. Stat. Sol.,* 2004, **8,** 1976

[7] A. Yoshikawa, T. Akagia, M. Nikl, N. Solovieva, K. Lebbou, C. Dujardin, C. Pedrini, T. Fukuda, *Nucle. Instr. Metho. Phys. Res. A,* 2002,**486**, 79

[8] S. Kaveh, C. P. Tremblay, N. Norhashim, R. J. Curry, A. K. Cheetham, *Adv. Mater.,* 2013, **25**, 6448

[9] S. Ye, F. Xiao, Y. X. Pan, Y. Y. Ma, Q. Y. Zhang, *Mater. Sci. Eng. R,* 2010, **71**, 1

[10] A. Kitai, *John Wiley & Sons, Ltd ISBN,* **2008**, 978-0-470-05818-3

[11] W. B. Im, N. George, J. Kurzman, S. Brinkley, A. Mikhailovsky, J. Hu, B. F. Chmelka, S. P. DenBaars, R. Seshadri, *Adv. Mater.,* 2011, **23**, 2300

[12] Y. Shimomura, T. Honma, M. Shigeiwa, T. Akai, K. Okamoto, N. Kijima, *J. Elect. Soc.,* 2007 **154**, 35

[13] A. A. Setlur, W. J. Heward, Y. Gao, A. M. Srivastava, R. G. Chandran, M. V. Shankar, *Chem. Mater.,* 2006, **18**, 3314

[14] J. K. Li, J.G. Li, S.H. Liu, X. D. Li, X. D. Sun, O. Sakkab, *J. Mater. Chem. C,* 2013, **1**, 7614

[15] J. M. Phillips, M. E. Coltrin, M. H. Crawford, A. J. Fischer, M. R. Krames, R. M. Mach, G. O. Mueller, Y. Ohno, L. E. S. Rohwer, J. A. Simmons, J. Y. Tsao, *Laser & Photon. Rev.,* 2007, ***1***, ***4***, 307

[16] W. B. Im, S. Brinkley, J. Hu, A. Mikhailovsky, S. P. Denbaars, R. Seshadri, *Chem. Mater.,* 2010, **22,** 2849

[17] C. K. Chang, T. M. Chen, *Appl. Phys. Lett.,* 2007, **90,** 161901

[18] H. S. Jang, Y. H. Won, D.Y. Jeon, *Appl. Phys. B,* 2009, **95,** 715

[19] C. M. Liu, Z. M. Qi, C. G. Ma, P. Dorenbos, D. J. Hou, S. Zhang, X. J. Kuang, J. H. Zhang, H. B. Liang, *Chem. Mater.,* 2006, **18,** 3709
[20] V. Singh, R. P. S. Chakradhar, J. L. Rao, and H. Y. Kwak, *Appl. Phys. B*, 2010 **98**(2–3), 407
[21] Z. F. Mu, Y. H. Hu, H. Y. Wu, C. J. Fu, and F. W. Kang, *Physica B*, 2011, **406**(4), 864.
[22] Z. G. Xia, J. Zhou, Z. Y. Mao, *J. Mater. Chem. C*, 2013**, 1,** 5917
[23] C. Y. Liu, Z.G. Xia, Z. P. Lian, J. Zhou, Q. F. Yan, *J. Mater. Chem. C*, 2013, **1,** 7139
[24] D. G. Deng, H. Yu, Y.Q. Li, Y. J. Hua, G. H. Jia, S. L. Zhao, H. P. Wang, L. H. Huang, Y. Y. Li, C. X. Li, S. Q. Xu, *J. Mater. Chem. C,* 2013**, 1,** 3194
[25] I. O. Galuskina, E. V. Galuskin, K. Prusik, V. M.Gazeev, N. N. Pertsev, P. Dzierzanowski, *Miner. Magaz.,* 2013, **7(6)**, 2857
[26] Z. Rak, R. C. Ewing, U. Becker, *Phys. Rev. B,* 2011, **83**, 155123
[27] I. O. Galuskina, E.V. Galuskin, P. Dzierżanowski, V. M. Gazeev, K. Prusik, N. Pertsev, A. Winiarski, A. E. Zadov, R. Wrzalik, *Am. Miner.,* 2010, **95,** 1305
[28] C. H. Huang, T. M. Chen, *J. Phys. Chem. C,* 2011,**115,** 2349
[29] D. L. Geng, M. M. Shang, Y. Zhang, H. Z. Lian, Z. Y. Cheng, J. Lin, *J. Mater. Chem. C,* 2013, **1,** 2345
[30] D. L. Geng, M. M. Shang, Y. Zhang, H. Z. Lian, J. Lin, *Inorg. Chem*. 2013, **52**, 13708
[31] H. Jing, C. F. Guo, G. G. Zhang, X. Y. Su, Z. Yang, J. H. Jeong, *J. Mater. Chem*., 2012, **22**, 13612
[32] H. H. Lin, H. B. Liang, B. Han, J. P. Zhong, Q. Su, P. Dorenbos, M. D. Birowosuto, G. B. Zhang, Y. B. Fu, W. Q. Wu, *Phys. Rev. B* 2007, **76**, 035117
[33] J. F. Sun, Z. P. Lian, G. Q. Shen, D.Z. Shen, *RSC Adv.,* 2013, **3**, 18395
[34] W. Y. Huang, F. Yoshimura, K. Ueda, Y. Shimomura, H. S. Sheu, T. S. Chan, C. Y. Chiang, W. Z. Zhou, R. S. Liu, *Chem. Mater.,* 2014, **26 (6)**, 2075
[35] P. Pust, V. Weiler, C. Hecht, A. Tücks, A. S. Wochnik, A. K. Henß, D. Wiechert, C. Scheu, P. J. Schmidt, W. Schnick, *Nat. Mater.,* 2014, **13**, 891
[36] Y. Q. Li, N. Hirosaki, R. J. Xie, T. Takeda, M. Mitomo, *Chem. Mater.,* 2008, **20,** 6704
[37] J. Chen, Y. G. Liu, H. K. Liu, D. X. Yang, H. Ding, M. H. Fang, Z. H. Huang, *Rsc. Adv.,* 2014, **01**, 1
[38] S. P. Lee, C. H. Huang, T. S. Chan, T. M. Chen, *Appl. Mater. Interfaces.,* 2014, **6 (10),** 7260

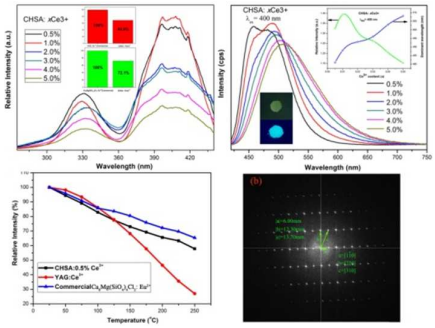

A new garnet compound phosphor $Ca_3Hf_2SiAl_2O_{12}$: xCe^{3+} is synthesized and it takes on nice photoluminescence properties.